

Film thickness distribution in gravity-driven pancake-shaped droplets rising in a Hele-Shaw cell

Isha Shukla¹, Nicolas Kofman¹, Gioele Balestra¹, Lailai Zhu^{1,2,3}
and François Gallaire^{1,†}

¹Laboratory of Fluid Mechanics and Instabilities, École Polytechnique Fédérale de Lausanne, 1015 Lausanne, Switzerland

²Department of Mechanical and Aerospace Engineering, Princeton University, Princeton, NJ 08544, USA

³Linné Flow Centre and Swedish e-Science Research Centre (SeRC), KTH Mechanics, SE-100 44 Stockholm, Sweden

(Received 27 December 2018; revised 29 May 2019; accepted 31 May 2019;
first published online 15 July 2019)

We study here experimentally, numerically and using a lubrication approach, the shape, velocity and lubrication film thickness distribution of a droplet rising in a vertical Hele-Shaw cell. The droplet is surrounded by a stationary immiscible fluid and moves purely due to buoyancy. A low density difference between the two media helps to operate in a regime with capillary number Ca lying between 0.03 and 0.35, where $Ca = \mu_o U_d / \gamma$ is built with the surrounding oil viscosity μ_o , the droplet velocity U_d and surface tension γ . The experimental data show that in this regime the droplet velocity is not influenced by the thickness of the thin lubricating film and the dynamic meniscus. For iso-viscous cases, experimental and three-dimensional numerical results of the film thickness distribution agree well with each other. The mean film thickness is well captured by the Aussillous & Quéré (*Phys. Fluids*, vol. 12 (10), 2000, pp. 2367–2371) model with fitting parameters. The droplet also exhibits the ‘catamaran’ shape that has been identified experimentally for a pressure-driven counterpart (Huerre *et al.*, *Phys. Rev. Lett.*, vol. 115 (6), 2015, 064501). This pattern has been rationalized using a two-dimensional lubrication equation. In particular, we show that this peculiar film thickness distribution is intrinsically related to the anisotropy of the fluxes induced by the droplet’s motion.

Key words: drops, Hele-Shaw flows, lubrication theory

1. Introduction

Transport of droplets and bubbles in confined environments is a common process in engineering applications, such as microscale heat transfer and cooling using a slug flow (Kandlikar 2012; Magnini, Pulvirenti & Thome 2013), enhanced oil recovery based on foam injections where bubbles move in porous media (Farajzadeh, Andrianov & Zitha 2009), and microfluidic engineering using droplets as micro-reactors

† Email address for correspondence: francois.gallaire@epfl.ch

(Song, Chen & Ismagilov 2006) and cell-encapsulating micro-compartments (He *et al.* 2005), to name a few. The study of transported droplets in confined dimensions also extends to biological science, where red blood cells traversing passages with non-axisymmetric geometries were analysed (Halpern & Secomb 1992).

Pioneering work has been initiated for a long bubble translating inside a straight cylindrical tube by Taylor (1961) conducting experiments and Bretherton (1961) combining experiments and asymptotic analysis. The analysis of Bretherton showed that the lubrication equations, at a very small capillary number Ca , were similar to their one-dimensional (1-D) version assuming spanwise invariance. He established the famous asymptotic relation between the uniform film thickness H_∞ and the capillary number in the $Ca < 10^{-3}$ regime, namely, $H_\infty/W = P(3Ca)^{2/3}/2$, where W is the tube diameter and P is a coefficient. The capillary number $Ca = \mu_o U_d / \gamma$ is built with the carrier phase dynamic viscosity μ_o , the droplet velocity U_d and the surface tension γ between the two fluids. Aussillous & Quéré (2000) proposed

$$\frac{H_\infty}{W} = \frac{1}{2} \frac{P(3Ca)^{2/3}}{1 + PQ(3Ca)^{2/3}}, \quad (1.1)$$

as the Taylor's law including an empirical coefficient $Q = 2.5$, with the coefficient P inherited from Bretherton (1961); this law was validated against the experimental data of Taylor (1961) for $Ca < 2$. The empirical relation was rationalized by incorporating into the analysis of Bretherton the so-called 'tube-fitting' condition, namely, that the bubble–film combination should fit inside the tube (Klaseboer, Gupta & Manica 2014). Besides those works considering the steady translation, Yu *et al.* (2018) have recently investigated how the lubrication film evolves between two steady states of a Bretherton bubble by combining theory, experiments and simulations.

Contrary to the translating bubble in a capillary tube, a bubble moving in a Hele-Shaw cell (two closely gapped parallel plates) resembles a flattened pancake. This configuration is relevant to microfluidic applications (Baroud, Gallaire & Dangla 2010) where the thickness of the microfluidic chips is much smaller than their horizontal dimension. Owing to the mathematical similarity between the governing equations of the depth-averaged Hele-Shaw flow and those of the two-dimensional (2-D) irrotational flow, as proved by Stokes (1898) and commented upon by Lamb (1993), potential flow theory was adopted to study the motion of a Hele-Shaw bubble theoretically (Taylor & Saffman 1959) and numerically (Tanveer 1986). Based on the stress jump derived by Bretherton (1961) and Park & Homsy (1984), 2-D depth-averaged simulations including the leading-order effects of the dynamic meniscus were also carried out (Meiburg 1989).

Motivated by the applications of droplet-based microfluidics, several works have recently been conducted to investigate the dynamics of a pressure-driven Hele-Shaw droplet. Huerre *et al.* (2015) and Reichert *et al.* (2018) performed high-precision experiments using the reflection interference contrast microscopy technique to study pressure-driven droplets, observing the so-called 'catamaran' droplet shape. Simulations based on a finite volume method (Ling *et al.* 2016) and a boundary integral method (BIM) (Zhu & Gallaire 2016) were carried out, confirming such a peculiar interfacial feature. It has to be mentioned that the much earlier work of Burgess & Foster (1990) performing a multi-region asymptotic analysis subtly revealed this feature for a Hele-Shaw bubble, which went rather unnoticed.

Limited work has been conducted for the gravity-driven droplets in a Hele-Shaw cell. Eri & Okumura (2011) and Yahashi, Kimoto & Okumura (2016) studied such

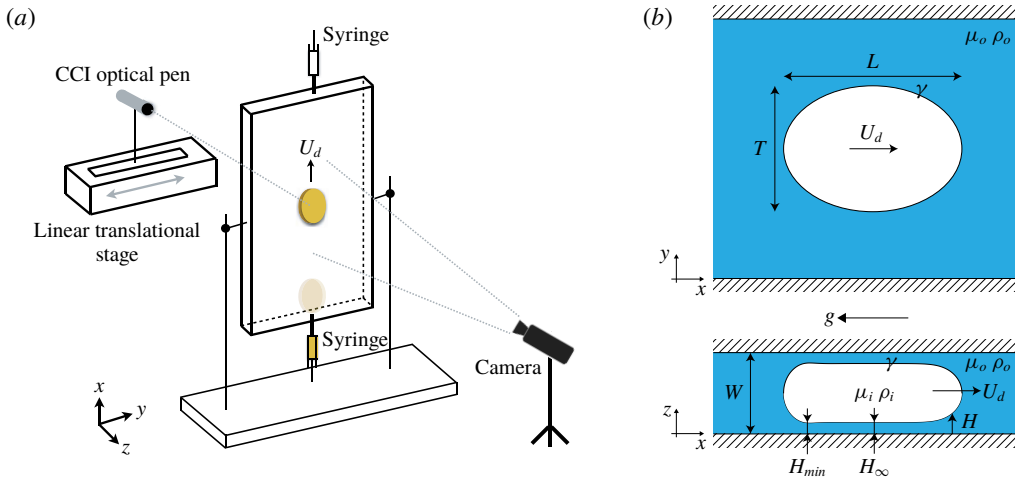


FIGURE 1. (Colour online) (a) Schematic of the experimental set-up. (b) Sketch of the problem: a droplet with density ρ_i and dynamic viscosity μ_i moving at velocity U_d in a Hele-Shaw cell of height W , where the carrier phase has a dynamic viscosity μ_o and its density $\rho_o > \rho_i$. The in-plane (x, y) projection shows the drop's longitudinal and transverse lengths, L and T , respectively. The out-of-plane (x, z) drop shape shows the thickness H_∞ of the uniform thin film and the minimum thickness H_{min} of the film along the centreline.

configurations experimentally, trying to build up the scaling laws for the viscous drag friction of the Hele-Shaw droplets. Recently, Keiser *et al.* (2018) conducted experiments to study a sedimenting Hele-Shaw droplet, focusing on its velocity as a function of confinement, viscosity contrast and the lubrication capacity of the carrier phase.

In this work, we combine experiments, simulations and a lubrication model solved numerically to study the buoyancy-driven translation of a droplet inside a vertical Hele-Shaw cell. We examine the droplet velocity, film thickness and how they vary with the density and viscosity difference between the droplet and carrier phase. We introduce the experimental set-up in §2, followed by the experimental results of the droplet mean velocity and film thickness in §§3.1 and 3.2, respectively. The comparison between the three-dimensional (3-D) BIM simulations and the experiments is shown in §3.3. The lubrication equation employed to model the problem is presented in §4, where the numerical solution of the lubrication equation is compared to the 3-D simulation results in §4.1. The film thickness pattern is rationalized by solving the linearized 2-D lubrication equation, which is presented in §4.2. We finally summarize our results in §5 with some discussions.

2. Experimental set-up

A vertical Hele-Shaw cell made of two parallel glass plates, separated by a gap W , is filled with silicone oil of dynamic viscosity 560 mPa s and density 972 kg m⁻³, measured at 20°C. An oil drop is injected into the silicone oil medium from the bottom using a syringe as shown in figure 1(a). The drop moves as a result of buoyancy. The higher the density difference between the inner and outer medium, the higher the drop velocity U_d . The spanwise and streamwise cell dimensions are sufficiently large compared to the drop size to avoid any finite size effects from the

Inner oil	μ_i (mPa s)	ρ_i (kg m ⁻³)	γ (mN m ⁻¹)
Linseed oil	49	929	2.88
Sunflower oil	69.5	921.5	2.73
Sesame oil	71	919.1	2.64
Olive oil	79.3	913.3	2.55
Peanut oil	83.8	913.3	3.11
Ricin oil (type 1) + 10% ethanol	302	943.1	4.97
Ricin oil (type 2) + 10% ethanol	322	943.3	4.46

TABLE 1. Dynamic viscosity μ_i and density ρ_i of the inner oils. Those of the outer oil are $\mu_o = 560$ mPa s and $\rho_o = 972$ kg m⁻³, except for the case of ricin (type 2) + 10% ethanol, for which the outer oil has $\mu_o = 319$ mPa s and $\rho_o = 970.5$ kg m⁻³. The interfacial surface tension between the inner–outer oils is γ . These properties were obtained at a room temperature of 20 °C.

lateral walls. On the other hand, the droplet is highly confined in the wall-normal direction. The droplet radius a is always larger than the cell gap W . Given the compliance of the glass walls, the thickness of which is bounded by our optical measurement tools, the cell gap W lies in the range of [4.59–4.8] mm and is recorded every time before the drop injection (see table 2).

The injected oils are tested beforehand to ensure non-wetting conditions for the oil droplet on the cell plates. The outer silicone oil totally wets the glass plate and forms a thin film of thickness H , between the drop and the glass's interface (see figure 1*b*), which is measured using a confocal chromatic imaging (CCI) optical pen (see details in appendix A). The pen is either placed fixed such that it measures the film thickness only along the centreline L (centreline film thickness) or mounted on a linear translational stage to perform lateral scans while the drop moves longitudinally. With an acquisition frequency of 200–500 Hz, scanning amplitude of 20–30 mm and frequency of 2–3 Hz, the obtained experimental data are interpolated in MATLAB to obtain the film thickness maps for the entire drop. Droplet size and velocity determine the optimal acquisition frequency for the thickness sensor, and the scanning amplitude and frequency for the linear translational stage.

We observe that for the chosen inner oil volumetric range, the droplet in-plane shape is no longer a circle but closer to an oval; hence we refer to the drop longitudinal length (along the direction of gravity) as L and to the transverse length as T , as shown in figure 1*b*). The drop motion is captured using a Phantom Miro M310 camera with a Nikon 105 mm macro lens. The spatio-temporal analysis of the movie ensures uniform drop velocity as the drop moves along a longitudinal distance of $5L$ or more.

The drop volume Q is expressed as a pancake of radius a and height $W - 2H_\infty$, where H_∞ is the mean film thickness. We can simplify Q as $\pi a^2 W$ when $H_\infty \ll W$. For the volumetric range used for the inner oils, we found that the longitudinal and transverse lengths, L and T , scale as the pancake radius a . The aspect ratio α is expressed as the ratio a/W . Keeping the cell gap W fixed, data for different aspect ratios are obtained using three different volumes (0.5 ml, 1 ml and 1.5 ml) for each oil.

Six oils with physical properties as mentioned in table 1 are used. The surface tension γ between the inner and outer media is measured using a Teclis tensiometer, and the oil viscosity and density are measured using an Anton Paar SVMTM 3000 viscometer. The experiment is performed at 20–22 °C.

Symbol	Definition	Expression	Working range
W	Cell gap	—	4.59–4.8 mm
U_d	Drop velocity	—	0.4–1.6 mm s ⁻¹
Q	Injected drop volume	—	0.44–1.5 ml
a	Pancake equivalent radius	$\sqrt{Q/\pi W}$	5.8–10.3 mm
α	Aspect ratio	a/W	1.25–2.27
$\Delta\rho$	Density difference	$ \rho_i - \rho_o $	27.3–58.8 kg m ⁻³
μ_i	Dynamic viscosity – droplet	—	49–322 mPa s
μ_o	Dynamic viscosity – outer medium	—	319–560 mPa s
γ	Interfacial surface tension	—	2.5–5.0 mN m ⁻¹
λ	Dynamic viscosity ratio	μ_i/μ_o	0.09–1.01
Ca	Capillary number	$\mu_o U_d/\gamma$	0.03–0.35
Bo	Bond number	$\Delta\rho g a^2/\gamma$	1.8–23.3

TABLE 2. List of notation, definitions and working ranges.

The ratio λ between the dynamic viscosity of the inner and outer phase lies in the range [0.09–0.54]. In addition to this range, another set of experiments is performed with $\lambda = 1.01$, where the outer medium is silicone oil ($\mu_o = 319$ mPa s, $\rho_o = 970.5$ kg m⁻³) and the inner medium is a mixture of ricin oil and 10% ethanol ($\mu_i = 322$ mPa s, $\rho_i = 943.3$ kg m⁻³) for three different drop volumes. The interfacial surface tension between these oils is 4.46 mN m⁻¹. The notation for the physical parameters and their definitions is detailed in table 2.

3. Experimental acquisition of the drop characteristics and their comparison with 3-D BIM simulations

3.1. Experimental results for drop velocity

Considering the bulk dissipation only, the resulting viscous drag force acting on the drop scales as $F_d \sim (\mu_i + \mu_o)U_d\pi a^2W^{-1}$. Unlike Okumura (2018), we consider both the inner and outer viscosities since they are of the same order. Balancing the total drag force with the buoyancy force, $F_g \sim \Delta\rho g\pi a^2W$, we obtain a scaling for the droplet mean velocity as

$$U_d \sim \frac{\Delta\rho g W^2}{(\mu_i + \mu_o)}, \quad (3.1)$$

where $\Delta\rho$ is the density difference and $g = 9.81$ m s⁻².

Under the assumption of cylindrical penny-shaped wetting drops, a theoretical expression for the drop velocity can be obtained from Maxworthy (1986), Bush (1997) and Gallaire *et al.* (2014). Gallaire *et al.* (2014) deduced the drop velocity in a Hele-Shaw cell, subjected to both buoyancy and Marangoni flow, using depth-averaged Stokes equations, called the Brinkman equations. In the absence of the Marangoni effect and at leading order, Bush (1997) and Gallaire *et al.* (2014) predicted the mean drop velocity as

$$U_d = \frac{\Delta\rho g W^2}{12\mu_o(\lambda + 1)}. \quad (3.2)$$

Introducing the Bond number Bo (see table 2), we can rewrite (3.2) using the aspect ratio α as

$$12\alpha^2(\lambda + 1)Ca = Bo. \quad (3.3)$$

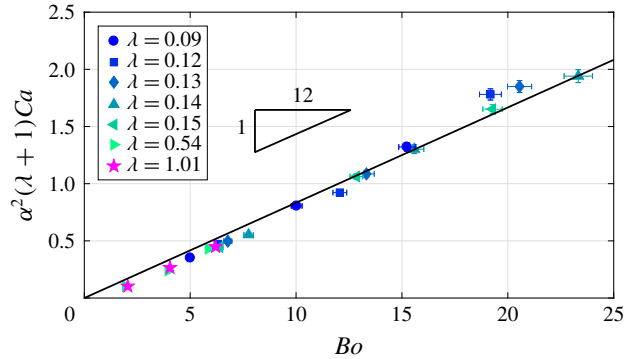


FIGURE 2. (Colour online) Experimental data $\alpha^2(\lambda + 1)Ca$ versus the Bond number Bo , where $Ca \in [0.03, 0.35]$. The markers correspond to different viscosity ratios λ of the inner–outer medium. The data closely fit (3.3) represented by the straight line.

The experimental data are plotted against the theoretical equation (3.3) in figure 2. Following the trend predicted by (3.3), figure 2 signifies that the dominant forces in play are buoyancy and viscous drag due to the volume of fluid displaced by the drop. The dissipation induced in the thin film as well as that in the dynamic meniscus region are found not to play a role in the selected parameter range. However, it has been observed that, for low Ca ranges, the dissipation in the thin film (Keiser *et al.* 2018) and in the dynamic meniscus (Reyssat 2014) have to be taken into account.

3.2. Experimental results for film thickness

Film thickness maps were measured for different droplet velocities. Since the thickness sensor fails to capture the data in the presence of high thickness gradient, no data are acquired along the drop edges, as shown in figure 3(d), where the black curve represents the drop in-plane boundary. For different aspect ratios, qualitatively similar thickness maps were obtained, with a high film thickness on the front edge, a constant film thickness in the centre and very low film thickness along the lateral edges of the drop, overall resembling a catamaran-like shape. The spanwise and streamwise cut made along the film thickness are shown in figure 3(b,c). The centreline film thickness indicated by the streamwise cut at $y = 0$ (figure 3b) clearly shows a monotonically decreasing film thickness pattern, followed by a region of constant film thickness H_∞ , which then reaches a minimum value of H_{min} . At the rear of the droplet, the strong thickness gradient reverses direction, to have an increasing thickness profile close to the drop receding edge, thus posing technical issues to capture the film thickness.

A similar centreline film thickness profile was obtained for all the droplets with a distinct value of H_∞ and H_{min} . These profiles are very similar to those of Bretherton (1961) for pressure-driven droplets, and as already noted in other works on pancakes (Huerre *et al.* 2015; Zhu & Gallaire 2016; Reichert *et al.* 2018). Non-dimensionalizing the mean and minimum values along the centreline using the cell gap W and plotting them as a function of Ca shows a saturating trend for higher Ca (figure 4). The experimental data are fitted based on the Taylor’s law model (Taylor 1961; Aussillous & Quéré 2000), according to which, apart from the static and dynamic meniscus regions, the lubrication film has a constant thickness of H_∞

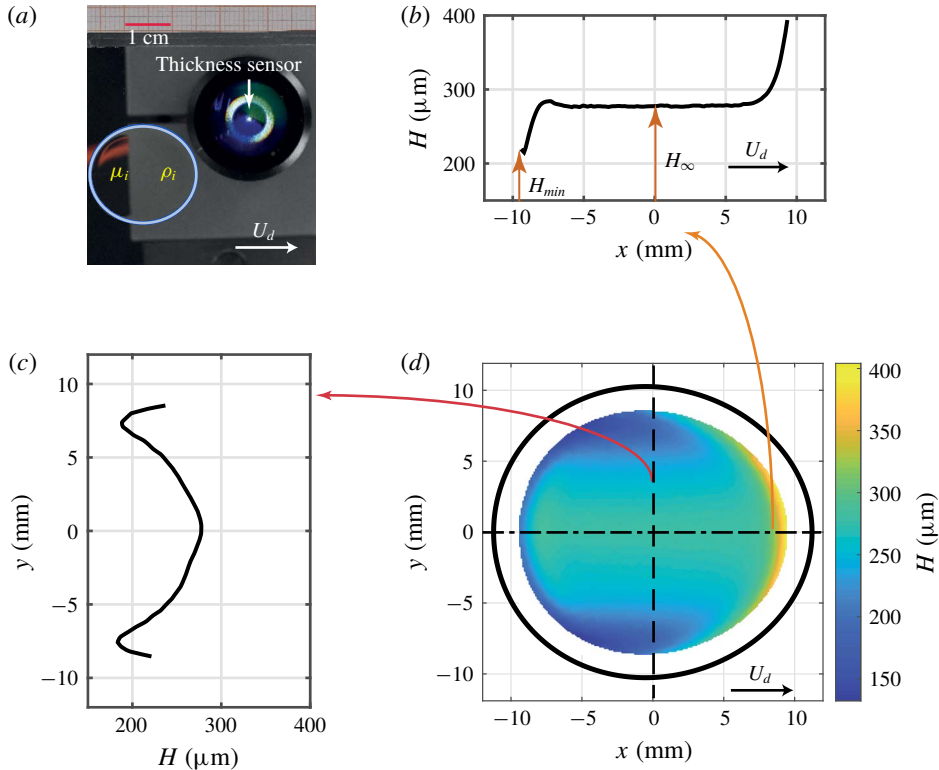


FIGURE 3. (Colour online) Drop characteristics for a droplet with $\lambda \sim 1$ moving with mean velocity $U_d = 0.64 \text{ mm s}^{-1}$, $Ca = 4 \times 10^{-2}$ and $Bo = 6.2$. (a) The blue curve shows the in-plane drop shape fitting based on (3.5) with $L/2 = 11.22 \text{ mm}$, $T/2 = 10.21 \text{ mm}$ and fitting coefficient $c = -7.485 \times 10^{-6} \text{ mm}^{-1}$. The film thickness in the streamwise and spanwise directions $y = 0$ and $x = 0$ of the drop are shown in (b) and (c), respectively. (b) The typical centreline thickness profile with monotonically decreasing thickness, followed by constant thickness H_∞ and ending with the minimum film thickness H_{min} . (c) The film thickness profile along the spanwise direction highlights the two minima along the lateral edge of the drop at $y \sim \pm 7.5 \text{ mm}$, which are clearly seen in panel (d), where we see the in-plane shape in black and the obtained film thickness map. The data are missing along the drop boundaries due to the presence of high thickness gradient that cannot be captured by the thickness sensor.

given as

$$\frac{H_\infty}{W} = \frac{1}{2} \frac{P(3Ca)^{2/3}}{1 + PQ(3Ca)^{2/3}}, \quad (3.4)$$

where the coefficients $P = 0.544$ and $Q = 2.061$ are obtained from the best-fitting curve for the experimental data. The nonlinear equation (3.4) is fitted using the MATLAB function *sseval* such that the objective function, defined as the sum of squared errors between the real data of H_∞/W and those predicted by (3.4), using any pair of parameters P and Q , is the minimum. The L_2 error norm for H_∞/W between the fitted and actual data is 0.02.

The fitting coefficients compare well with those of Aussillous & Quéré (2000) and Klaseboer *et al.* (2014), where the mean film thickness model for bubbles

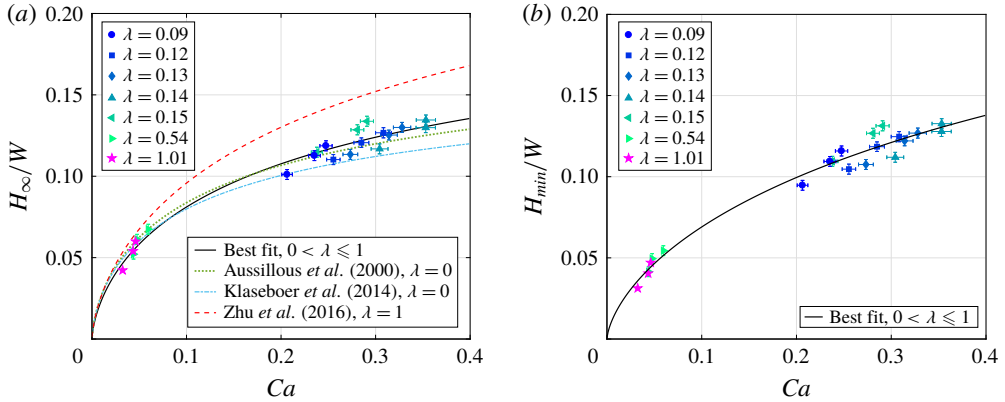


FIGURE 4. (Colour online) (a) Dimensionless mean (H_∞/W) and (b) minimum (H_{min}/W) film thickness, as functions of Ca . The black curve represents the best-fitting curve obtained using the Taylor's law model with $P = 0.544$ and $Q = 2.061$ for H_∞/W and with $P = 0.372$ and $Q = 1.247$ for H_{min}/W . For the mean film thickness, predictions based on the coefficients P and Q from the Taylor's law (Aussillous & Qu  r   2000; Klaseboer *et al.* 2014; Zhu & Gallaire 2016) are also shown.

($\lambda = 0$) is based on the Taylor's law with coefficient $P = 0.643$, and $Q = 2.5$ and 2.79 , respectively. Fitting coefficients obtained from a 3-D BIM simulation of Zhu & Gallaire (2016) for pressure-driven flows and $\lambda = 1$ show the same order of magnitude as the experimental ones, with $P = 0.6$ and $Q = 1.5$.

In figure 4(a), we see that our experimental data for mean film thickness are bounded by the predicted values for the two extreme viscosity ratios of $\lambda = 0$ and $\lambda = 1$. Comparing the thickness predictions by Klaseboer *et al.* (2014) and Zhu & Gallaire (2016) for $Ca = 0.1$, we see that the thickness variation is 20% as λ increases from 0 to 1. This is consistent with the 18% (approximately) increase as reported in Martinez & Udell (1990) for pressure-driven drops in an axisymmetric tube. Further, this variation in thickness reduces to a merely 11% for $Ca = 0.05$, as λ changes from 0 to 1.

The same model when used for fitting the minimum film thickness profile H_{min}/W gives fitting coefficients $P = 0.372$ and $Q = 1.247$ with an $L2$ error norm between the fitted and actual data as 0.025.

Motivated by the qualitative agreement for the mean film thickness value between the experimental data and the 3-D BIM simulations for pressure-driven droplets (figure 4a), we perform a 3-D BIM simulation using the solver developed in Zhu & Gallaire (2016), suitably adapted for gravity-driven droplets. The reader is referred to that paper for details of the numerical scheme.

3.3. Comparison with 3-D simulations

The current numerical simulations only address the cases where the inner and outer viscosities are the same, namely $\lambda = 1$. To realize it experimentally, three different drop volumes, 0.44 ml, 1 ml and 1.5 ml, were injected into the Hele-Shaw cell, resulting in $Ca = 0.032$, 0.043 and 0.046, with the corresponding $Bo = 1.81$, 4.04 and 6.2. The error in volume injected decreased from 10% to 3% as we moved from the smallest to the largest drop volume.

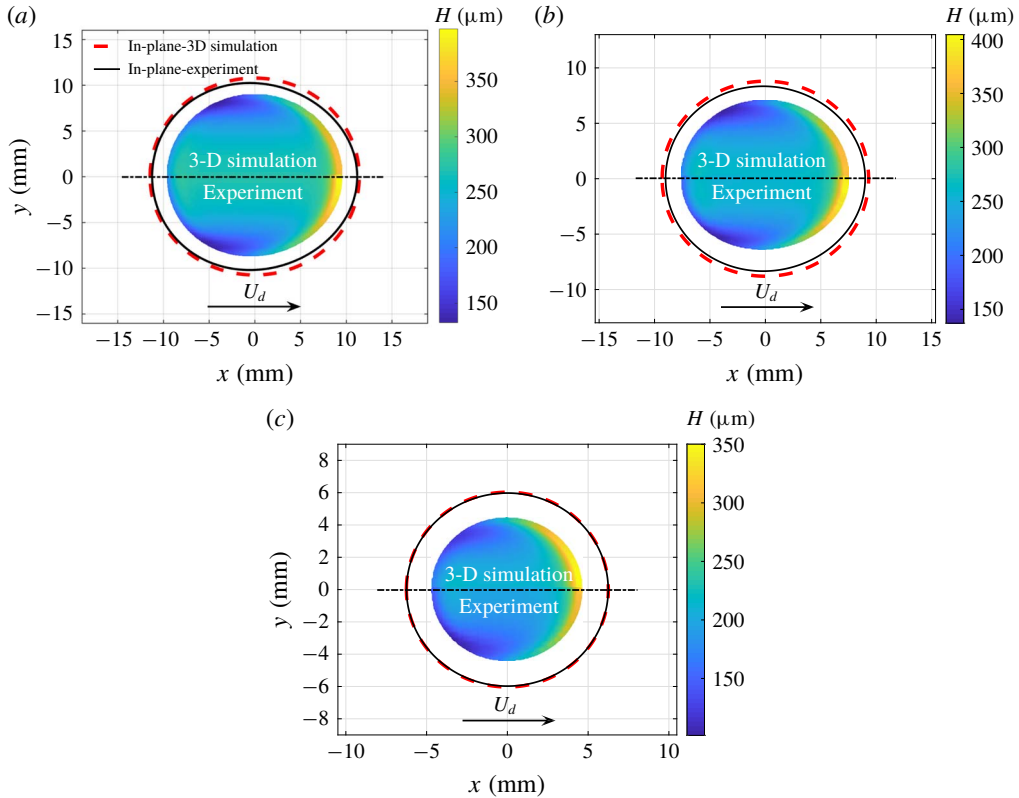


FIGURE 5. (Colour online) Film thickness map whose top (respectively bottom) half corresponds to the 3-D BIM (experimental) data for three drop volumes: (a) 1.5 ml ($Ca = 0.046$, $Bo = 6.2$); (b) 1 ml ($Ca = 0.043$, $Bo = 4.04$); and (c) 0.44 ml ($Ca = 0.032$, $Bo = 1.81$). The viscosity ratio $\lambda \approx 1$. The experimental and numerical in-plane shapes are represented by black and red dashed curves, respectively. The numerical results for H_∞ along the centreline deviate from the experimental data by 2%, 3% and 5%, respectively, for the three cases.

The experimental film thickness maps for the chosen Ca range show that the precise shape of the pancake in-plane shape is close to an oval. Hence, the experimental in-plane drop shape is obtained by fitting the following equation

$$\frac{x^2}{(L/2)^2} + \frac{y^2}{(T/2)^2} e^{cx} = 0, \quad (3.5)$$

on an instantaneous image of the drop, where c is a fitting parameter (figure 3a).

Experimentally, due to the large thickness gradient along the drop edges, the CCI sensor fails to capture the thickness in these regions. Thus the map is obtained for an area smaller than the in-plane shape of the drop (black curve in figure 5). In contrast, the numerical simulations are capable of retrieving the complete film thickness map; however, to make a visually effective comparison between the experiments and numerics, only the part of the numerical result with the same area as the experimental data is shown in figure 5. Its top (bottom) half corresponds to the

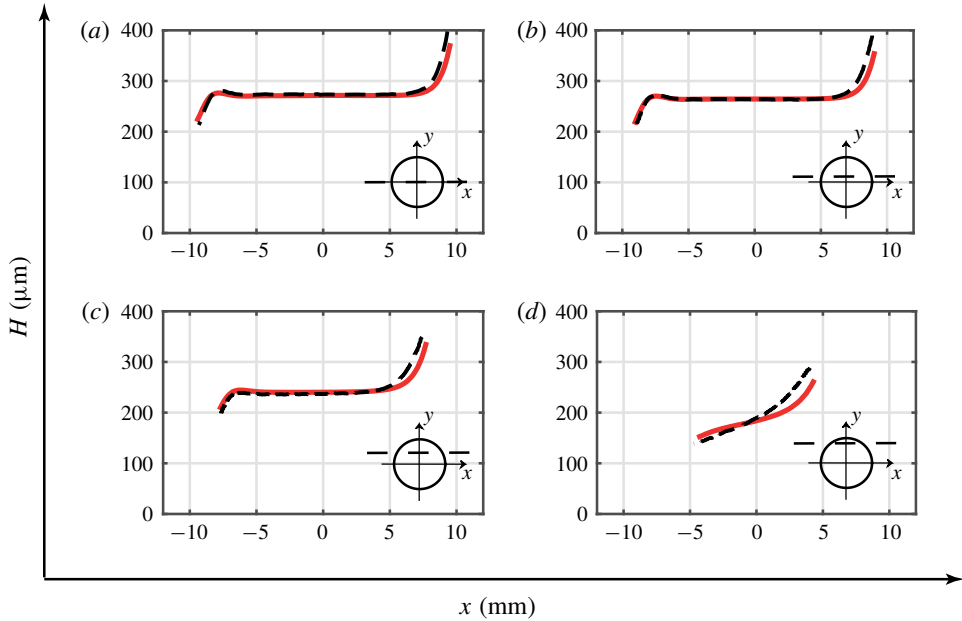


FIGURE 6. (Colour online) Film thickness cuts made along the streamwise directions at (a) $y = 0$, (b) $y = 2.5$ mm, (c) $y = 5$ mm and (d) $y = 7.5$ mm, where $Ca = 0.046$ and $Bo = 6.2$. Black dashed lines represent the experimental results and red lines the numerical predictions. The decrease in the film thickness towards the lateral edges can be observed by comparing panels (a) and (d), where the mean film thickness decreases by around 30% signifying the appearance of catamarans close to $(x, y) \approx (-4, 7.5)$ mm.

numerical (experimental) data, respectively. The red dashed curve refers to the numerical in-plane shape of the drop.

Both the experiments and simulations capture the formation of catamarans at the lateral transition regions, a uniform film thickness in the centre and a very high film thickness at the front edge of the drop. The agreement is almost quantitative. The relative error in the uniform film thickness H_∞ for drop volumes 0.44 ml, 1 ml and 1.5 ml is 5%, 3% and 2%, with absolute values of 12 μm , 7 μm and 6 μm , respectively.

The numerical solution is further validated by making several streamwise (figure 6) and spanwise (figure 7) cuts along the largest drop of volume 1.5 ml. Along the centreline, the 3-D BIM simulation captures precisely the lubrication film variation: large film thickness at the front edge, followed by a constant thickness profile, ending in a small oscillation before posing an increasing trend at the rear edge. There is a good quantitative comparison between the experiments and numerics, with a slight variation in the film thickness along the advancing meniscus.

4. Analysis of the film thickness pattern

In order to rationalize the film thickness pattern observed in § 3.3, hereafter we model the problem using a lubrication approach. For simplicity, we formulate the 2-D lubrication equation assuming the drop dynamic viscosity $\mu_i = 0$.

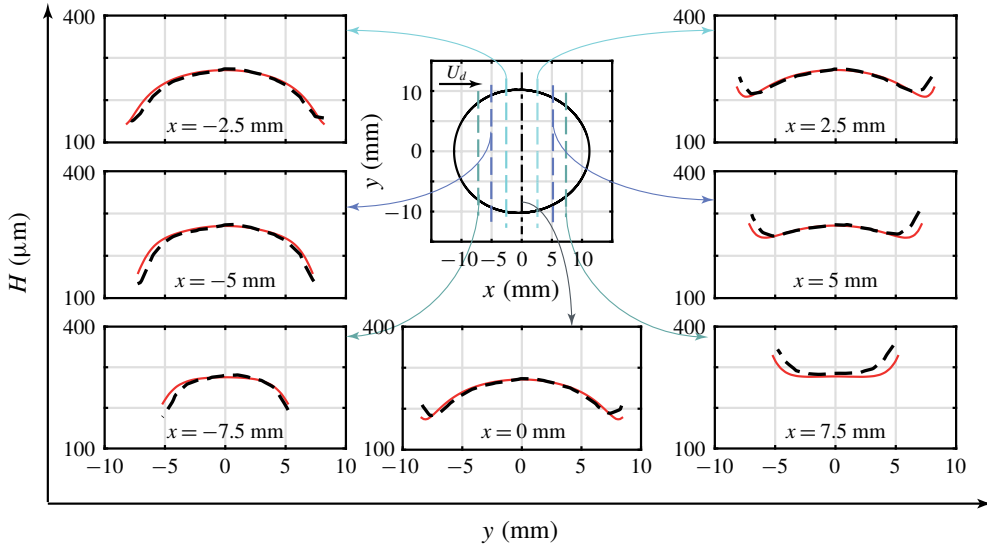


FIGURE 7. (Colour online) Film thickness variation along the spanwise directions at $x = 0$, $x = \pm 2.5$ mm, $x = \pm 5$ mm and $x = \pm 7.5$ mm, where $Ca = 0.046$ and $Bo = 6.2$. Black dashed lines represent the experimental results and red lines the numerical results. Transverse cuts enclosed by the region $x = -2.5$ mm to $x = -5$ mm highlight the minima in the lubrication film along the lateral edges.

4.1. Formulating the nonlinear 2-D lubrication equation

Applying the long-wavelength assumption (Oron, Davis & Bankoff 1997) and by neglecting inertia, the 2-D nonlinear lubrication equation (see details in appendix B) for the film thickness H separating the interface from the wall, in the reference frame moving at the drop velocity U_d , can be derived. Using the pancake radius a as the characteristic length and a/U_d as the characteristic time, the dimensionless lubrication equation for the steady profile in the dimensionless coordinate system \bar{x} , \bar{y} is written as

$$\frac{\partial}{\partial \bar{x}} \left[\bar{H}^3 \left(\frac{1}{3Ca} \bar{\kappa}_x - \frac{Bo}{3Ca} \right) - \bar{H} \right] + \frac{\partial}{\partial \bar{y}} \left(\bar{H}^3 \frac{1}{3Ca} \bar{\kappa}_y \right) = 0, \quad (4.1)$$

where $\bar{\kappa}$ is the mean curvature of the interface, given by $\bar{\kappa} = \nabla \cdot \mathbf{n}$, where the unit normal vector \mathbf{n} on the interface is given by

$$\mathbf{n} = \frac{(-\bar{H}_x, -\bar{H}_y, 1)^T}{\sqrt{1 + \bar{H}_x^2 + \bar{H}_y^2}}. \quad (4.2)$$

Note the anisotropy of the fluxes in (4.1): both the buoyancy and the motion in the \bar{x} direction do not affect the flux in the \bar{y} direction, breaking the isotropy induced by the capillary pressure gradient.

The nonlinear equation (4.1) together with the equation for the interface curvature $\bar{\kappa}$ are solved numerically by the commercial finite element solver COMSOL Multiphysics. The two variables for this coupled system of partial differential equations are \bar{H} and $\bar{\kappa}$. As boundary conditions we impose the film thickness $\bar{H} = W/2a$ and the mean curvature $\bar{\kappa} = \bar{\kappa}_{f,r}$ at the droplet mid-height. The mean curvature boundary condition in the static meniscus is composed by a component in

the (\bar{r}, θ) plane and a component in the (\bar{r}, \bar{z}) plane. In the spirit of Meiburg (1989) and Nagel (2014), we consider the local capillary number defined with the normal velocity to the static cap for the mean curvature boundary condition model:

$$\bar{\kappa}_{f,r}(\bar{r}, \theta) = \underbrace{\frac{2a}{W} \left(\frac{1 + T_{f,r}(3Ca |\cos \theta|)^{2/3}}{1 + Z_{f,r}(3Ca |\cos \theta|)^{2/3}} \right)}_{(\bar{r}, \bar{z}) \text{ plane}} + \underbrace{\frac{\pi}{4} \frac{1}{\bar{r}}}_{(\bar{r}, \theta) \text{ plane}}, \quad (4.3)$$

where coefficients with subscript f have to be used for $\theta \in [-\pi/2, \pi/2]$ and those with subscript r for $\theta \in [\pi/2, 3\pi/2]$, where θ and \bar{r} are defined as $\theta = \arctan(\bar{y}/\bar{x})$ and $\bar{r} = (\bar{x}^2 + \bar{y}^2)^{1/2}$, respectively. The values of the coefficients are $T_f = 2.285$, $T_r = -0.5067$, $Z_f = 0.4075$ and $Z_r = -0.1062$. The curvature boundary condition model in the (\bar{r}, \bar{z}) plane is inspired by the equivalent model of Balestra, Zhu & Gallaire (2018), which has been developed by an extensive study for the 2-D planar Stokes problem. The validity of this model has recently been corroborated by Atasi *et al.* (2018) for pancake bubbles. The correction $\pi/4$ for the in-plane curvature $1/\bar{r}$ in the (\bar{r}, θ) plane, where $\bar{r} = 1$ for a circular geometry, has been derived asymptotically by Park & Homsy (1984). Note that a more involved model could be used to describe the out-of-plane curvature ((\bar{r}, \bar{z}) plane) in the lateral transition regions (Burgess & Foster 1990).

In the present work we extract the pancake shape from the results of the 3-D BIM simulations for $\lambda = 1$. As explained in § 3.3, the in-plane boundaries of the deformed pancake in the (\bar{r}, θ) plane can be well described by (3.5).

It has to be stressed that the used lubrication equation should not, *a priori*, be used in the static meniscus region close to the boundary, where the interface slope is large. However, we have found that such an approach gives surprisingly good results if one uses the model for the static rim curvature (4.3) for the curvature boundary condition (see Balestra (2018) for a discussion of the axisymmetric case), which directly sets the film thickness profile in that region. Hence, such an approach can be used to numerically obtain the film thickness profile over the entire domain, also behind its validity range.

The comparison between the film thickness profile obtained by the solution of the nonlinear lubrication equation using the model equation (4.3) for the static cap mean curvature $\bar{\kappa}_{f,r}(r, \theta)$, with the one obtained by the 3-D BIM simulations, is shown in figure 8. One can observe that both methods predict the formation of catamarans at the lateral transition regions, a uniform film thickness in the centre and oscillations at the back. In spite of the strong assumptions made for this model, the agreement is surprisingly good, even with an iso-viscous drop ($\mu_i = \mu_o$). The relative error in the uniform film thickness is 10% and its absolute value is 30 μm . The thin-film pattern shown by both approaches, as well as by the experiments, is therefore indeed a robust feature. Supported by this agreement, we investigate the thin-film pattern using the linearized version of this simple 2-D lubrication model, which is computationally much cheaper than the 3-D Stokes simulations.

4.2. Qualitative analysis of thickness pattern using the linearized 2-D lubrication equation

The qualitative nature of the film thickness pattern can be inferred by performing a linear analysis of the 2-D lubrication equation (4.1). With the use of the film thickness

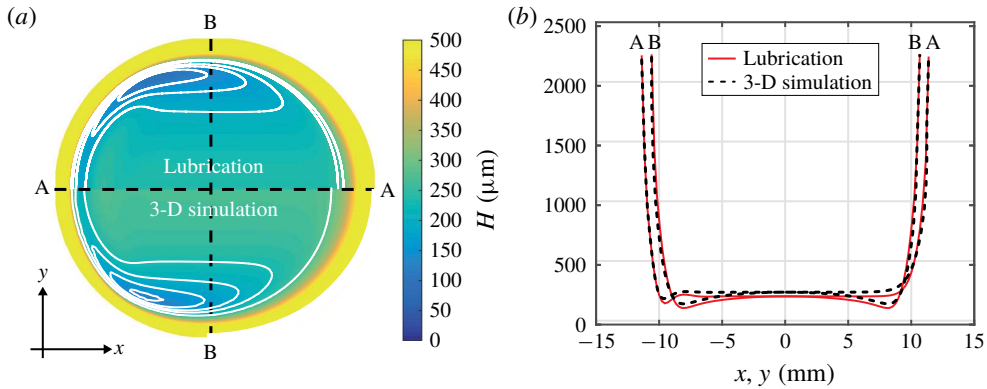


FIGURE 8. (Colour online) (a) Comparison between the solution of the nonlinear lubrication equation assuming $\lambda = 0$ (top half) and that of the 3-D BIM simulations assuming $\lambda = 1$ (bottom half), where $Ca = 4.6 \times 10^{-2}$ and $Bo = 6.2$. (b) Comparison for cuts made along the streamwise direction A–A and spanwise direction B–B.

decomposition $\bar{H} = \bar{H}_\infty + \varepsilon h$, where $\bar{H}_\infty = H_\infty/a$, the linear equation for the first-order film thickness correction reads:

$$\frac{\bar{H}_\infty^3}{3Ca} \underbrace{(h_{xxxx} + 2h_{xyxy} + h_{yyyy})}_{\Delta^2 h} - \left(1 + \frac{\bar{H}_\infty^2 Bo}{Ca}\right) h_x = 0. \quad (4.4)$$

The film thickness \bar{H}_∞ is expressed using the empirical model (3.4) (Taylor 1961; Aussillous & Quéré 2000; Balestra *et al.* 2018), with $P = 0.643$ and $Q = 2.2$.

Equation (4.4) for the film thickness correction around the uniform film thickness \bar{H}_∞ can be solved as a boundary-value problem, as recently conducted by Atasi *et al.* (2018). In contrast to the nonlinear solution of § 4.1, here we only solve the lubrication equation from the thin-film region up to the beginning of the dynamic meniscus region. This is equivalent to looking at the first-order correction of the uniform thin-film region due to the matching of the film thickness in the dynamic meniscus region to a larger value. In the present context, we impose a film thickness correction $h = A$ and a mean curvature of the order $\Delta h = 1/A + 1/\bar{r}$ on the perimeter, with A as a constant value of $10^{-3} \times \bar{H}_\infty$. This boundary condition does not have to be understood as a rigorous matching approach, but rather as a way to find the structure of the film thickness profile in the region where it is close to being uniform. A rigorous matching for the limit $Ca \ll 1$ can be found in Park & Homsy (1984). The maps of the film thickness correction h , together with some profiles along the streamwise and spanwise directions, are shown in figure 9.

First, it can be clearly observed that the linear lubrication equation with a perturbed film thickness and curvature along the domain boundary is able to reproduce the catamaran-like pattern observed in pancake droplets as seen in §§ 4.1 and 3.3. The film thickness is the smallest in the lateral part of the pancake (see figure 9a), so that its 3-D shape resembles the hull of a catamaran. Therefore, we can conclude that this pattern is the generalization of the 1-D oscillations found by Bretherton (1961) at the rear of an axisymmetric bubble for a 2-D concave structure, like a pancake droplet, and is intrinsically related to the anisotropy of the equation.

Second, the film thickness correction along the streamwise direction \bar{x} (see figure 9c) deviates from a uniform profile as expected from Bretherton's theory (Bretherton

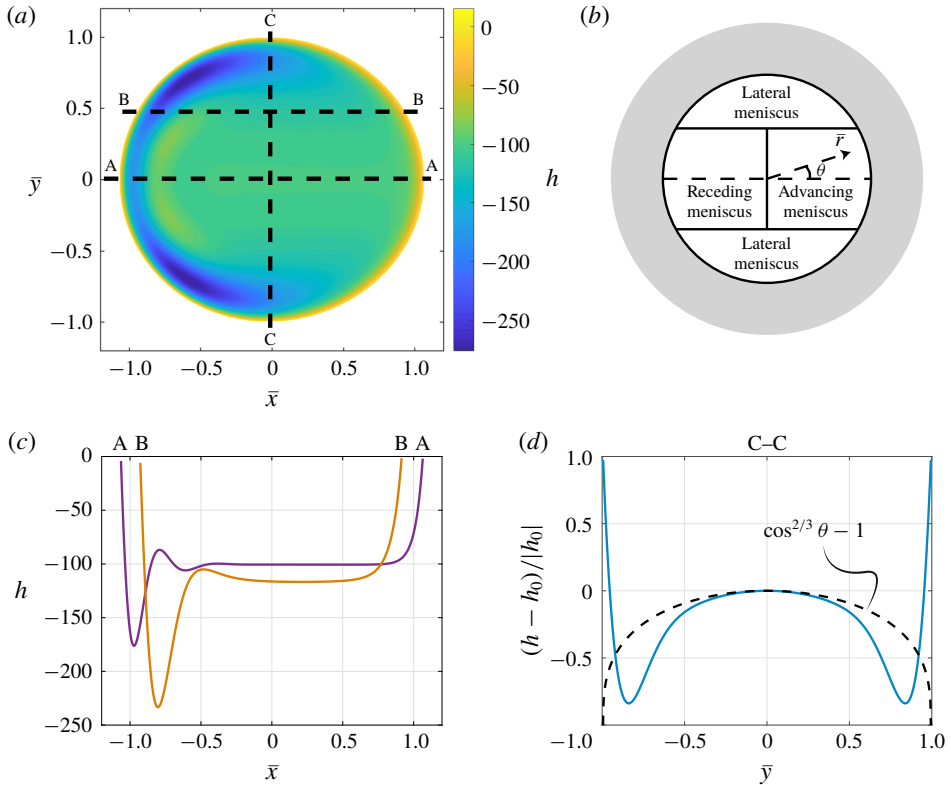


FIGURE 9. (Colour online) Linear film thickness correction h around the uniform film thickness \bar{H}_∞ for a pancake droplet (a,c,d). The film thickness correction map is shown in (a), the cuts along the streamwise direction at two different \bar{y} locations are plotted in (c) and the normalized difference of the film thickness correction along the spanwise cut C–C with respect to $h_0 = h(\bar{y} = 0)$ along this cut is shown in (d), where the law $(\cos \theta)^{2/3}$ is indicated by the black dashed line. Here $A = 10^{-3} \times \bar{H}_\infty$, $Ca = 4.6 \times 10^{-2}$, $Bo = 6.2$ and $\alpha = 2.2$. The polar coordinates (\bar{r}, θ) are introduced and the boundaries are highlighted by the grey area in panel (b).

1961). The film thickness oscillates at the rear meniscus and increases monotonically at the front meniscus. Note that the film thickness correction in the uniform film region of a pancake is not vanishing, as the base film thickness \bar{H}_∞ is given by (3.4), which is an asymptotic estimate for $Bo = 0$ but not an exact solution of the lubrication equation with $Bo \neq 0$. Furthermore, it can be observed that the more one moves away from $\bar{y} = 0$, the more the thickness of the film is reduced. Therefore, the thickness of the film left by the front meniscus is not uniform.

To better highlight this crucial point, we show in figure 9(d) the normalized difference between the film thickness correction and its value at $\bar{y} = 0$. The film thickness decreases as $|\bar{y}|$ increases, before increasing again close to the edge to match the boundary condition.

These qualitative observations can be rationalized by simplifying the linear lubrication equation (4.4) for the different regions of the domain (see figure 9b). The lubrication equation (4.4) in polar coordinates can be simplified to

$$\frac{\bar{H}_\infty^3}{3Ca} h_{\bar{r}\bar{r}\bar{r}} - \left(1 + \frac{\bar{H}_\infty^2 Bo}{Ca}\right) \left(\cos \theta h_{\bar{r}} - \frac{\sin \theta}{\bar{r}} h_\theta\right) = 0. \tag{4.5}$$

For small polar angles θ , the contribution $(\sin \theta / \bar{r}) h_\theta$, which corresponds to the flux in the tangential direction, can be neglected so that the linear lubrication equation becomes, after integration along \bar{r} ,

$$h_{\bar{r}\bar{r}} = K_p h, \tag{4.6}$$

with

$$K_p = \left(\frac{3Ca}{\bar{H}_\infty^3} + \frac{3Bo}{\bar{H}_\infty}\right) \cos \theta, \tag{4.7}$$

which is the linearized 1-D equation for the Landau–Levich–Derjaguin–Bretherton problem (Landau & Levich 1942; Derjaguin 1943; Bretherton 1961) in the radial direction \bar{r} projected on the streamwise direction. Therefore, we know from the solution of Bretherton (1961) that the film thickness is oscillating at the rear meniscus and monotonically increasing at the front one. Focusing for now on $Bo = 0$, we know that the thickness deposited by a front meniscus depends on the velocity normal to the interface. In this case, one has therefore $\bar{H}_\infty \sim Ca_p^{2/3}$ with $Ca_p = Ca \cos \theta$ as the local capillary number at a given polar angle θ . Hence, the film thickness in the central region of the pancake varies like $(Ca \cos \theta)^{2/3}$. Similar results have been reported for a pressure-driven red blood cell traversing a non-axisymmetric passage (Halpern & Secomb 1992) and in pancake droplets by Reichert *et al.* (2018). Once a given film thickness is set by the front meniscus, the same thickness will be present over the entire thin-film region at the corresponding spanwise location \bar{y} . The good agreement between the dependence on $(\cos \theta)^{2/3}$ of the film thickness and the profile along the spanwise direction obtained by resolving the 2-D lubrication equation is shown in figure 9(d).

Similarly, the oscillations at the rear meniscus depend on the polar angle. For a pancake droplet, due to the film thickness non-uniformity resulting from the non-uniform deposition at the front, the wavelength of the oscillations at the back scales as $\lambda_{osc} \sim (Ca \cos \theta)^{1/3}$. Given the 1/3 power-law dependence, the wavelength is almost unchanged, before rapidly reducing to 0 when $\theta \rightarrow \pm\pi/2$ (see figure 9a).

It is important to note that a plane cut of the film thickness at a given angle θ does not present a region of constant film thickness. A pancake droplet cannot be seen just as the collection of different 1-D profiles obtained by the solution to (4.6) for different polar angles θ . In fact, the film thickness at any spanwise location \bar{y} is set by the front meniscus at the corresponding polar angle θ and (4.6) only indicates the scaling of this film thickness as well as the oscillations at the back.

For $\theta \rightarrow \pm\pi/2$, which corresponds to the lateral meniscus region (see figure 9b), the tangential flux term $(\sin \theta / \bar{r}) h_\theta$ in (4.5) can no longer be neglected. Burgess & Foster (1990) performed an involved analysis of the lubrication equation in this region for a pancake droplet at low capillary numbers and found that the local film thickness in the so-called lateral transition regions scales as $Ca^{4/5}$ rather than as $Ca^{2/3}$. Therefore, for $Ca \ll 1$, the film thickness in these lateral regions is much smaller than that in the other regions. This explains why one observes catamaran-like structures in the lateral regions of pancake droplets. Note that, for the Ca range considered in the present study, the film thickness in the lateral transition regions is still sufficiently large so that the viscous dissipation can be neglected also in these regions, as confirmed by the results of § 3. Furthermore, Burgess & Foster (1990) have also shown that the polar extent of these lateral regions scales as $Ca^{1/5}$, whereas their radial extent scales as $Ca^{2/5}$ instead of as $Ca^{1/3}$ that one has for the length of the rear and front dynamic menisci of axisymmetric droplets (see also Hodges, Jensen & Rallison 2004).

5. Conclusions and perspectives

We report the velocity, mean film thickness and thickness map for a droplet moving due to buoyancy in a vertical Hele-Shaw cell. The mean drop velocity compares well with the leading-order velocity expression of Gallaire *et al.* (2014). This signifies that buoyancy and viscous drag force are the dominant forces in our experimental parameter range, with the viscous dissipation in the film thickness and in the dynamical meniscus having a negligible effect on the droplet velocity. On the contrary, the dimensionless mean film thickness data were dependent on the dimensionless droplet velocity, expressed as Ca , and were fitted with the Taylor's law model (Aussillous & Quéré 2000).

We also obtained the complete film thickness maps using a CCI optical pen mounted on a linear translation stage. Based on a boundary integral method, 3-D Stokes equations were solved. These numerical results for $\lambda = 1$ were in very good agreement with our experimental results. The thickness pattern had a distinct catamaran-like shape as experimentally observed for pressure-driven flows in Huerre *et al.* (2015) and Reichert *et al.* (2018).

To understand the nature of the thickness patterns observed experimentally and numerically, the problem was approached using a lubrication equation, which was solved as a boundary-value problem, rather than as an initial-value problem, as recently conducted by Atasi *et al.* (2018). In spite of all the crude assumptions made in developing the model, its nonlinear solution for the film thickness profile of a pancake bubble compared surprisingly well with the results of 3-D BIM simulations, evidencing the robustness of the thin-film pattern.

In order to unravel the structure of the film thickness profile, we linearized the lubrication model and solved for the linear thickness corrections around a uniformly thick film. We have been able to show that not only the oscillations at the rear meniscus, but also the catamaran-like pattern, can be directly retrieved by solving the linear 2-D lubrication equation when perturbing the film thickness at the boundaries, which mimics the presence of a meniscus of greater film thickness. In particular, the catamaran-like structure results from the anisotropic flux induced by the motion of the walls with respect to the pancake and the need to match the film thickness to larger values in the dynamic meniscus region surrounding the region where the thin film is rather uniform. This pattern is therefore independent of the force driving the motion. In fact, in totally different contexts, the same pattern is also found in drops levitating on a moving substrate (Hodges *et al.* 2004; Lhuissier *et al.* 2013) as well as in oleoplaning drops (Daniel *et al.* 2017). In the central part of the pancake droplet, the thickness left by the front meniscus scales as $(Ca \cos \theta)^{2/3}$, and depends therefore on the velocity normal to the interface. This scaling no longer holds in the lateral transition region, where the component of the flux tangential to the interface becomes important and the thickness of the film is much smaller, resulting in the formation of the catamaran-like structure.

Finally, we would like to highlight a contrasting feature seen between drops moving in a cylindrical tube and that in a Hele-Shaw cell. In cylindrical tubes the main difference between the pressure-driven and buoyancy-driven bubble motion, as found by Bretherton (1961), is that buoyant bubbles may remain stuck if the capillary radius is less than $0.918l_c$, where the capillary length $l_c = \sqrt{\gamma/\Delta\rho g}$. This failure results from the impossibility to match the static gravity-corrected meniscus shape with the flat thin-film region. A similar result was obtained recently in the planar geometry by Lamstaes & Eggers (2017) with a prefactor of 0.847. Interestingly enough, we suspect that there is no such bubble arrest in Hele-Shaw cells, as a

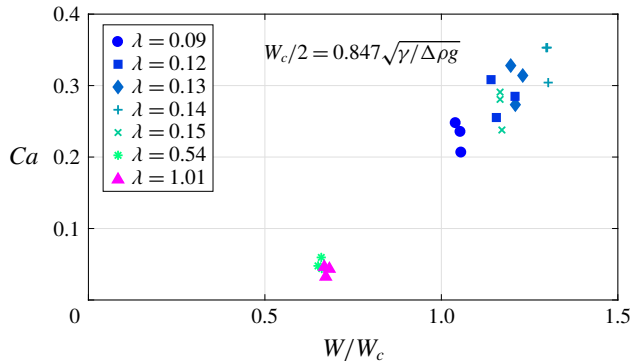


FIGURE 10. (Colour online) As stated by Lamstaes & Eggers (2017), for a planar geometry the drops should get stuck when $W < W_c$. Our experiments show that the pancake-shaped drops continue to move beyond this limitation.

consequence of the additional direction which adds a degree of freedom in the curvature. As shown in figure 10, our experimental results show marked drop motion when the half cell gap is below $0.847l_c$.

Acknowledgements

I.S. thanks the Swiss National Science Foundation (grant no. 200021-159957). The computer time was provided by the Swiss National Supercomputing Centre (CSCS) under project ID s603. An ERC starting grant ‘SimCoMiCs 280117’ is gratefully acknowledged. L.Z. is grateful for a VR International Postdoc Grant ‘2015-06334’ from the Swedish Research Council. We thank Ludovic Keiser for fruitful discussions.

Appendix A. CCI working principle

We hereby describe the principle of the confocal chromatic imaging (CCI) technique. An achromatic lens decomposes the incident white light into a continuum of monochromatic images, which constitutes the measurement range. The light reflected by a sample surface put inside this range is collected by a beam splitter. A pinhole then allows one to block the defocused light that does not come from the sample surface. Eventually, the spectral repartition of the collected light is analysed by a spectrometer. The wavelength of maximum intensity is detected and the distance value is deduced from a calibration curve. Several reflecting interfaces can be detected at the same time, allowing thickness measurement of thin transparent layers.

Appendix B. Derivation of 2-D nonlinear lubrication equation for pancake droplets

The derivation of the model equation presented in §4.2 is briefly outlined here. Considering the same physical properties for the droplet and the outer medium as outlined in §1, and under the assumption of negligible inertia (Oron *et al.* 1997) with $\rho_i \ll \rho_o$ and $\mu_i \ll \mu_o$, the 3-D momentum equations reads

$$0 = -\frac{\partial p}{\partial x} + \mu_o \left(\frac{\partial^2 u}{\partial x^2} + \frac{\partial^2 u}{\partial y^2} + \frac{\partial^2 u}{\partial z^2} \right) - \rho_o g, \quad (\text{B } 1)$$

$$0 = -\frac{\partial p}{\partial y} + \mu_o \left(\frac{\partial^2 v}{\partial x^2} + \frac{\partial^2 v}{\partial y^2} + \frac{\partial^2 v}{\partial z^2} \right), \tag{B 2}$$

$$0 = -\frac{\partial p}{\partial z} + \mu_o \left(\frac{\partial^2 w}{\partial x^2} + \frac{\partial^2 w}{\partial y^2} + \frac{\partial^2 w}{\partial z^2} \right). \tag{B 3}$$

Using L as the characteristic length scale in the x and y directions and the film thickness H as the characteristic length scale in the z direction, the film aspect ratio ϵ is defined as $\epsilon = H/L$. The long-wavelength approximation is employed since $\epsilon \ll 1$. Mass conservation indicates that the characteristic velocity in the z direction (W) is much smaller than the other two components (U in x and V in y direction), $W \sim \epsilon U \ll U$ and $W \sim \epsilon V \ll V$. The Stokes equation simplifies as

$$0 = -\frac{\partial p}{\partial x} + \mu_o \frac{\partial^2 u}{\partial z^2} - \rho_o g, \tag{B 4}$$

$$0 = -\frac{\partial p}{\partial y} + \mu_o \frac{\partial^2 v}{\partial z^2}, \tag{B 5}$$

$$0 = -\frac{\partial p}{\partial z}. \tag{B 6}$$

Integrating equation (B 6) in z and applying dynamic boundary conditions yields $p = p_0 - \gamma\kappa$, where κ is the mean curvature of the interface. Integrating equations (B 4) and (B 5) twice in z and considering $u(z=0) = -U_d$ and the zero-slip boundary condition $v(z=0) = 0$, as well as the zero-shear-stress interface $\partial u(z=H)/\partial z = 0$ and $\partial v(z=H)/\partial z = 0$, yields the velocity components

$$u = \frac{(\gamma\kappa_x - \Delta\rho g)}{\mu_o} \left(H - \frac{z}{2} \right) z - U_d, \tag{B 7}$$

$$v = \frac{\gamma\kappa_y}{\mu_o} \left(H - \frac{z}{2} \right) z. \tag{B 8}$$

Since the inner medium density $\rho_i \ll \rho_o$, we replace ρ_o by $\Delta\rho$ in (B 7), where $\Delta\rho = \rho_o - \rho_i$ represents the density difference between the inner and outer fluids. Integrating equations (B 7) and (B 8) in z from 0 to H yields the flux in x and y directions as

$$Q^u = \frac{H^3}{3\mu_o} (\gamma\kappa_x - \Delta\rho g) - U_d H, \tag{B 9}$$

$$Q^v = \frac{H^3}{3\mu_o} \gamma\kappa_y. \tag{B 10}$$

Finally, integrating the continuity equation and applying the Leibniz integral rule and the kinematic boundary condition at the interface yields the mass conservation equation expressed as

$$\frac{\partial H}{\partial t} + \frac{\partial Q^u}{\partial x} + \frac{\partial Q^v}{\partial y} = 0. \tag{B 11}$$

Introducing equations (B 9) and (B 10) in (B 11) finally yields the lubrication equation

$$\frac{\partial H}{\partial t} + \frac{\partial}{\partial x} \left[\frac{H^3}{3\mu_o} \underbrace{(\gamma\kappa_x)}_{\text{I}} - \underbrace{(\Delta\rho g)}_{\text{II}} \right] - \underbrace{U_d H}_{\text{III}} + \frac{\partial}{\partial y} \left[\frac{H^3}{3\mu_o} \underbrace{\gamma\kappa_y}_{\text{I}} \right] = 0. \tag{B 12}$$

The terms I in the spatial variation of the flux correspond to the surface tension effects, term II to the variation due to the buoyancy force, and term III accounts for the reference frame moving with the drop. Note the anisotropy of the fluxes: both the buoyancy and the motion in the x direction do not affect the flux in the y direction, breaking the isotropy induced by the capillary pressure gradient.

Using the pancake radius a as the characteristic length and a/U_d as the characteristic time, the dimensionless lubrication equation for the steady profile in the dimensionless coordinate system \bar{x}, \bar{y} is written as (4.1).

REFERENCES

- ATASI, O., HAUT, B., DEHAECK, S., DEWANDRE, A., LEGENDRE, D. & SCHEID, B. 2018 How to measure the thickness of a lubrication film in a pancake bubble with a single snapshot? *Appl. Phys. Lett.* **113** (17), 173701.
- AUSSILLOUS, P. & QUÉRÉ, D. 2000 Quick deposition of a fluid on the wall of a tube. *Phys. Fluids* **12** (10), 2367–2371.
- BALESTRA, G. 2018 Pattern formation in thin liquid films: from coating-flow instabilities to microfluidic droplets. PhD thesis, EPFL, Lausanne.
- BALESTRA, G., ZHU, L. & GALLAIRE, F. 2018 Viscous Taylor droplets in axisymmetric and planar tubes: from Bretherton's theory to empirical models. *Microfluid. Nanofluid.* **22** (6), 67.
- BAROUD, C. N., GALLAIRE, F. & DANGLA, R. 2010 Dynamics of microfluidic droplets. *Lab on a Chip* **10** (16), 2032–2045.
- BRETHERTON, F. P. 1961 The motion of long bubbles in tubes. *J. Fluid Mech.* **10** (2), 166–188.
- BURGESS, D. & FOSTER, M. R. 1990 Analysis of the boundary conditions for a Hele-Shaw bubble. *Phys. Fluids A* **2** (7), 1105–1117.
- BUSH, J. W. M. 1997 The anomalous wake accompanying bubbles rising in a thin gap: a mechanically forced Marangoni flow. *J. Fluid Mech.* **352**, 283–303.
- DANIEL, D., TIMONEN, J. V. I., LI, R., VELLING, S. J. & AIZENBERG, J. 2017 Oleoplaning droplets on lubricated surfaces. *Nat. Phys.* **13** (10), 1020–1025.
- DERJAGUIN, B. V. C. R. 1943 Thickness of liquid layer adhering to walls of vessels on their emptying and the theory of photo- and motion-picture film coating. *C. R. (Dokl.) Acad. Sci. URSS* **39**, 13–16.
- ERI, A. & OKUMURA, K. 2011 Viscous drag friction acting on a fluid drop confined in between two plates. *Soft Matt.* **7** (12), 5648–5653.
- FARAJZADEH, R., ANDRIANOV, A. & ZITHA, P. L. J. 2009 Investigation of immiscible and miscible foam for enhancing oil recovery. *Ind. Engng Chem. Res.* **49** (4), 1910–1919.
- GALLAIRE, F., MELIGA, P., LAURE, P. & BAROUD, C. N. 2014 Marangoni induced force on a drop in a Hele-Shaw cell. *Phys. Fluids* **26** (6), 062105.
- HALPERN, D. & SECOMB, T. W. 1992 The squeezing of red blood cells through parallel-sided channels with near-minimal widths. *J. Fluid Mech.* **244**, 307–322.
- HE, M., EDGAR, J. S., JEFFRIES, G. D. M., LORENZ, R. M., SHELBY, J. P. & CHIU, D. T. 2005 Selective encapsulation of single cells and subcellular organelles into picoliter- and femtoliter-volume droplets. *Anal. Chem.* **77** (6), 1539–1544.
- HODGES, S. R., JENSEN, O. E. & RALLISON, J. M. 2004 Sliding, slipping and rolling: the sedimentation of a viscous drop down a gently inclined plane. *J. Fluid Mech.* **512**, 95–131.
- HUERRE, A., THEODOLY, O., LESHANSKY, A. M., VALIGNAT, M.-P., CANTAT, I. & JULLIEN, M.-C. 2015 Droplets in microchannels: dynamical properties of the lubrication film. *Phys. Rev. Lett.* **115** (6), 064501.
- KANDLIKAR, S. G. 2012 History, advances, and challenges in liquid flow and flow boiling heat transfer in microchannels: a critical review. *J. Heat Transfer* **134** (3), 034001.
- KEISER, L., JAAFAR, K., BICO, J. & REYSSAT, É. 2018 Dynamics of non-wetting drops confined in a Hele-Shaw cell. *J. Fluid Mech.* **845**, 245–262.

- KLASEBOER, E., GUPTA, R. & MANICA, R. 2014 An extended Bretherton model for long Taylor bubbles at moderate capillary numbers. *Phys. Fluids* **26** (3), 032107.
- LAMB, H. 1993 *Hydrodynamics*. Cambridge University Press.
- LAMSTAES, C. & EGGERS, J. 2017 Arrested bubble rise in a narrow tube. *J. Stat. Phys.* **167** (3–4), 656–682.
- LANDAU, L. & LEVICH, B. 1942 Dragging of a liquid by a moving plate. *Acta Physicochim. URSS* **17** (42), 42–54.
- LHUISSIER, H., TAGAWA, Y., TRAN, T. & SUN, C. 2013 Levitation of a drop over a moving surface. *J. Fluid Mech.* **733**, R4.
- LING, Y., FULLANA, J.-M., POPINET, S. & JOSSEERAND, C. 2016 Droplet migration in a Hele-Shaw cell: effect of the lubrication film on the droplet dynamics. *Phys. Fluids* **28** (6), 062001.
- MAGNINI, M., PULVIRENTI, B. & THOME, J. R. 2013 Numerical investigation of hydrodynamics and heat transfer of elongated bubbles during flow boiling in a microchannel. *Intl J. Heat Mass Transfer* **59**, 451–471.
- MARTINEZ, M. J. & UDELL, K. S. 1990 Axisymmetric creeping motion of drops through circular tubes. *J. Fluid Mech.* **210**, 565–591.
- MAXWORTHY, T. 1986 Bubble formation, motion and interaction in a Hele-Shaw cell. *J. Fluid Mech.* **173**, 95–114.
- MEIBURG, E. 1989 Bubbles in a Hele-Shaw cell: numerical simulation of three-dimensional effects. *Phys. Fluids A* **1** (6), 938–946.
- NAGEL, M. 2014 Modeling droplets flowing in microchannels. PhD thesis, EPFL, Lausanne.
- OKUMURA, K. 2018 Viscous dynamics of drops and bubbles in Hele-Shaw cells: drainage, drag friction, coalescence, and bursting. *Adv. Colloid Interface Sci.* **255**, 64–75.
- ORON, A., DAVIS, S. H. & BANKOFF, S. G. 1997 Long-scale evolution of thin liquid films. *Rev. Mod. Phys.* **69** (3), 931.
- PARK, C. W. & HOMS, G. M. 1984 Two-phase displacement in Hele-Shaw cells: theory. *J. Fluid Mech.* **139**, 291–308.
- REICHERT, B., HUERRE, A., THEODOLY, O., VALIGNAT, M.-P., CANTAT, I. & JULLIEN, M.-C. 2018 Topography of the lubrication film under a pancake droplet travelling in a Hele-Shaw cell. *J. Fluid Mech.* **850**, 708–732.
- REYSSAT, E. 2014 Drops and bubbles in wedges. *J. Fluid Mech.* **748**, 641–662.
- SONG, H., CHEN, D. L. & ISMAGILOV, R. F. 2006 Reactions in droplets in microfluidic channels. *Angew. Chem. Intl Ed. Engl.* **45** (44), 7336–7356.
- STOKES, G. G. 1898 Mathematical proof of the identity of the stream lines obtained by means of a viscous film with those of a perfect fluid moving in two dimensions. In *Report of the Sixty-Eighth Meeting of the British Association for the Advancement of Science*, pp. 143–144.
- TANVEER, S. 1986 The effect of surface tension on the shape of a Hele-Shaw cell bubble. *Phys. Fluids* **29** (11), 3537–3548.
- TAYLOR, G. I. & SAFFMAN, P. G. 1959 A note on the motion of bubbles in a Hele-Shaw cell and porous medium. *J. Mech. Appl. Maths* **12** (3), 265–279.
- TAYLOR, G. I. 1961 Deposition of a viscous fluid on the wall of a tube. *J. Fluid Mech.* **10** (2), 161–165.
- YAHASHI, M., KIMOTO, N. & OKUMURA, K. 2016 Scaling crossover in thin-film drag dynamics of fluid drops in the Hele-Shaw cell. *Sci. Rep.* **6**, 31395.
- YU, Y. E., ZHU, L., SHIM, S., EGGERS, J. & STONE, H. A. 2018 Time-dependent motion of a confined bubble in a tube: transition between two steady states. *J. Fluid Mech.* **857**, R4.
- ZHU, L. & GALLAIRE, F. 2016 A pancake droplet translating in a Hele-Shaw cell: lubrication film and flow field. *J. Fluid Mech.* **798**, 955–969.